A novel melt infiltration method promoting porosity development of low-rank coal derived activated carbon as supercapacitor electrode materials

Lijie Wang, Fei Sun*, Jihui Gao*, Xinxin Pi, Tong Pei, Zhipeng Qie, Guangbo Zhao, Yukun Qin

School of Energy Science and Engineering, Harbin Institute of Technology, Harbin 150001, Heilongjiang, China

A B S T R A C T

Focusing on the bottlenecks of traditional physical or chemical activation methods for the preparation of activated carbons, we report a simple and scalable melt infiltration strategy assisted with CO_2 activation for the preparation of activated carbons from Chinese large-scale reserve Zhundong coal. The preparation is achieved by the melt infiltration of a small amount of anhydrous $FeCl_3$ (10–20 wt%) into the coal framework and subsequent CO_2-assisted physical activation during which the encapsulated iron species play the dual role of pore-forming templates and activating catalysts. The as-obtained MI-AC-2 possesses a partially hierarchical pore structure with a high specific surface area of 1872 m^2 g^{-1}, five times more than the activated carbon prepared by solely physical activation, which endows the constructed MI-AC-2 electrode with good supercapacitive performances. Relative to the large consumption of activation agents used in a traditional chemical activation process, such a new method with low-cost resource materials and the low-dose $FeCl_3$ additive paves a scalable way to loading metal precursor into coal/biomass for the preparation of high-porosity activated carbons. This work also provides a simple and efficient strategy to encapsulate active materials into external matrix or substrate.

© 2018 Taiwan Institute of Chemical Engineers. Published by Elsevier B.V. All rights reserved.

1. Introduction

Carbonaceous materials, due to their high physicochemical compatibility, easily-tunable porosity and framework and environmentally benign nature, have been extensively explored and applied in the fields of gas adsorption [1–4], electrochemical energy storage [5–8] and catalysis [9–11]. To date, various types of carbonaceous materials such as graphite [12], activated carbons [2–5,9], ordered mesoporous carbons [13,14], carbon fibers [15], fullerene [16] and graphene [17,18] have shown progress in carbon materials science and engineering. Among them, activated carbons derived from various types of biomass/coals have the advantages of low-cost and facile production, thus inducing people to extend their applications from ancient times to the present [4,19].

Take supercapacitor as an example, it stores charges by the electrostatic adsorption or accumulation of electrolyte ions onto the surface of activated carbon electrodes [7]. According to the capacitance calculation equation ($C = \varepsilon S/d$), high porosity and large specific surface area (SSA) can promote the value of capacitance [20,21]. Hence, some high surface area activated carbons [22] or

heteroatom-doped activated carbons [19] were successfully synthesized based on controllable physical or chemical activation methods. These activated carbons show improvements in boosting the capacitance of constructed electrodes. However, the current physical or chemical activation methods for preparing activated carbons have two main bottlenecks. Firstly, traditional physical activation methods employing H_2O, CO_2, flue gas or their mixtures as activation agents often leads to the resulting activated carbons having low porosity and a specific surface area less than 1000 m^2 g^{-1} [2]. Secondly, frequently-used chemical activation process, producing high surface area activated carbon via adding a large amount of chemical activation agents (such as KOH [22,23], K_2CO_3 [24,25], $ZnCl_2$ [26] and H_3PO_4 [27]), it subsequently needs much water/acid consumption to remove the residual activation agents, which increases the difficulties of industrial-level production and environmental governance. Thus, it is desirable to develop new strategies for preparing high porosity/surface area activated carbons to overcome the weakness of traditional physical or chemical activation crafts.

Low-grade coals, featuring high reserve, medium calorific value, higher volatile matter and high reactivity, are superior precursor candidates for preparing activated carbons. For example, Zhundong coal in Chinese Xinjiang District has an exploitable reserve of 164 Gt and an unripe, easily-tunable coal framework [28]. In

our previous study, a one-step ammonia activation method was utilized to prepare Zhundong coal-derived N-doped microporous carbons which show excellent performances as gas adsorbents and electrochemical energy storage materials [1]. In this study, we demonstrated a novel melt infiltration method to promote the porosity development of Zhundong coal-based activated carbons. The preparation process involves the melt infiltration of anhydrous $FeCl_3$ into the coal framework and subsequent CO_2-assisted physical activation, during which the embedded iron species play the dual role of pore-forming templates and activating catalysts. Such a melt infiltration strategy endowed the resulting activated carbon (denoted as MI-AC-2) with a greatly increased specific surface area, five times more than that of the activated carbon (denoted as AC) produced by solely physical activation. Particularly noteworthy is that the mass fraction of $FeCl_3$ additive is only 10–20% of the coal precursor, much lower than the dose of activation agents used in the traditional chemical activation process. Evaluated as supercapacitor electrode materials, the as-obtained MI-AC-2 shows high capacitances, good rate capability and excellent cycling stability.

2. Experimental section

2.1. Synthesis of MI-ACs, AC and LI-AC

Zhundong coal, a kind of low-rank coal, is rich in humic acid structures that contain numerous side chains or functional groups linked to benzene rings. The proximate and ultimate analysis results for raw Zhundong coal are given in Table S1, indicating relatively high volatile component. The ash compositions for raw Zhundong coal are given in Table S2. For the synthesis of Zhundong coal based activated carbons, the raw coal with particle size less than 1 mm first underwent a hydrochloric acid (5 M) and hydrofluoric acid (20 wt%) treatment procedure with stirring at 50 °C for 12 h to remove the minerals [29]. As can be seen from Fig. S1, some less apparent peaks appeared in the XRD pattern of ZD coal, while the XRD pattern of ZD-HCF was relatively smooth without obvious peaks, which indicated that minerals in raw coal sample have been removed. For the synthesis of MI-ACs, a melt infiltration method was employed. In a typical procedure, anhydrous $FeCl_3$ (Aladdin) and coal powders with a certain mass ratio were mixed and grinded to get a homogeneous mixture, which was then transferred to a glass vial and vacuumized for 1 h. Subsequently, the vial was then sealed under vacuum and heat-treated at 350 °C for 1 h (Fig. S1). Because the molten and boiling point of anhydrous $FeCl_3$ is relatively low, which is 305 °C and 312 °C, molten or gasified anhydrous $FeCl_3$ could penetrate into the framework of coal sample by capillary force under high-temperature vacuum condition. After cooling down, the sample in the vial was transferred into a crucible in a horizontal furnace, which was then activated at 900 °C for 1 h under a mixture of CO_2 and N_2 atmosphere (including 120 mL min^{-1} N_2 and 80 mL min^{-1} CO_2) with a heating rate of 10 °C min^{-1}. During the CO_2-assisted activation, the entrapped and dispersible iron species could catalyze the reaction between coal skeleton and CO_2 and promote the pore formation. Then the activated samples underwent a washing (2 M HCl and de-ionized water) and drying procedure to yield the MI-ACs (Fig. S2). Some new pores were released during the removal of iron-based components in the process of washing. Compare with the traditional liquid impregnation, this method could ensure the formation of small Fe-containing crystals uniformly dispersed and confined in the coal inner structure, thus leading to the resulting activated carbon with high porosity. By changing the $FeCl_3$-to-coal mass ratio from 1:10, 2:10 to 3:10, in the melt infiltration process, MI-AC-1, MI-AC-2 and MI-AC-3 were prepared, respectively.

Control samples (AC and LI-AC) to demonstrate the melt infiltration effect on the porosity development of MI-ACs, a solely physi-

cal activation procedure (similar to the above process but without the melt infiltration steps) was used to obtain the activated carbon (denoted as AC) for comparison. Moreover, a liquid impregnation method was used to prepare the activated carbon (denoted as LI-AC). To be specific, a pre-weighed amount of mineral-free coal was added into the solution of $FeCl_3$ to make a coal-water slurry ($FeCl_3$-to-coal mass ratio of 1:5) during magnetic stirring. Then the coal-water slurry was dried at 80 °C with magnetic stirring of 300 r min^{-1} until the water completely evaporated. The obtained $FeCl_3$-coal mixture then underwent the same CO_2-assisted physical activation process as MI-ACs. A comparing schematic for illustrating the preparation process of $FeCl_3$-coal mixture between melt infiltration and liquid impregnation can be seen in Fig. S1.

2.2. Characterizations

Scanning electron microscopy (SEM, Helios Nanolab600i) with energy dispersive X-ray apparatus and transmission electron microscopy (TEM, JEM-2100) were adopted to record the morphology and inherent mineral distribution of the samples. N_2 adsorption/desorption isotherms of the resulting samples were measured at −196 °C using ASAP 2420 (V2.05) apparatus. The BET surface area was calculated from the isotherm according to the Brunauer–Emmett–Teller equation [22]. The micropore volume (V_{mic}) was estimated by the Horvath–Kawazoe (HK) method. The total pore volume (V_{total}) was calculated from the N_2 amount adsorbed at relative pressure of 0.975. Pore size distribution was calculated based on Density Functional Theory (DFT) [30]. X-ray diffraction (XRD) patterns were measured on a Rigaku D/Max 2400 diffractometer using CuKa radiation (40 kV, 40 mA, $\lambda = 1.5406$ Å). X-ray photoelectron spectroscopy (XPS) analysis was performed on a PHI 5700 ESCA System with Al Ka X-ray at 14 kV and 6 mA.

Thermogravimetric analysis (TGA) was conducted to record the weight loss of coal or coal-iron mixture by simulating CO_2-assisted physical activation process mentioned above. Typically, 10 mg of coal or coal-iron mixture was heated at a heating rate of 10 °C min^{-1} until 900 °C holding 1 h with a gas mixture of 40 mL min^{-1} CO_2 and 60 mL min^{-1} N_2 flowing through. Carbon conversion was calculated by the following equation [31]:

$$X_t = \frac{W_0 - W_t}{W_0 - W_{resi}} \tag{1}$$

Where X is carbon conversion, W_0 is the initial sample mass, W_t is the sample mass at the time of t, and W_{resi} is the mass of residual after activation process. Reactivity of coal was evaluated by the normalized reaction rate [32] as the following equation:

$$K_t = \frac{dX_t/dt}{1 - X_t} \tag{2}$$

Where K_t is the normalized reaction rate (min^{-1}), dX_t/dt is the reaction rate, and X_t is the carbon conversion at time t.

2.3. Fabrication of electrodes and electrochemical measurement

The electrochemical performances of the obtained activated carbons were determined in a three-electrode system with a basic aqueous solution (6 M KOH). For the fabrication of electrodes, the active material (80 wt%), carbon black (10 wt%), and polytetrafluoroethylene (PTFE) (10 wt%) were homogeneously mixed and rolled into a thin film. The above thin film was dried at 100 °C for 12 h and then pressed onto a nickel foam with a mass loading of 3 mg cm^{-2} as the working electrode. Pt foil and a saturated calomel electrode (SCE) electrode were used as the counter electrode and reference electrode, respectively [21]. All the electrochemical tests were conducted at room temperature. Galvanostatic charge/discharge (GC), cyclic voltammetry (CV), and electrical impedance spectroscopy (EIS) studies were all performed using
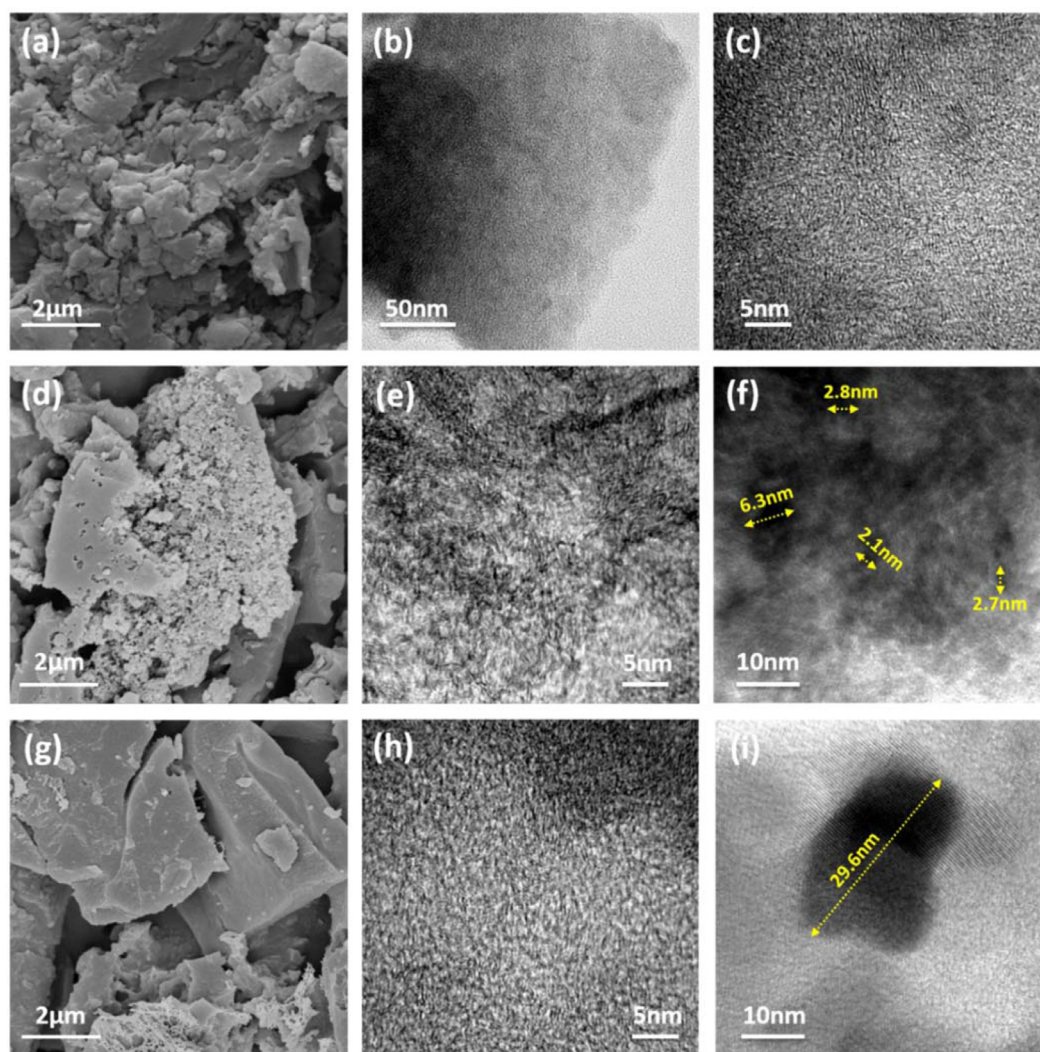
Fig. 1. SEM and TEM images of various samples: (a) SEM image of AC; (b) TEM image of AC; (c) HRTEM image of AC; (d) SEM image of MI-AC-2; (e) HRTEM image of MI-AC-2; (f) HRTEM image of pre-washed MI-AC-2 with iron species enclose; (g) SEM image of LI-AC; (h) HRTEM image of LI-AC; (i) HRTEM image of pre-washed LI-AC with iron species enclose.

CHI660E. The specific gravimetric capacitances (Cs, F g^{-1}) of the prepared samples were calculated based on the following formula Cs = $I\Delta t/(m\Delta V)$, where I is the constant discharge current, Δt is the time for a full discharge, m is the mass of active material in the working electrode, and ΔV represents voltage window (excluding the internal resistance (IR) drop) [7].

3. Results and discussion

3.1. Structural characterizations

Firstly, the structure characteristics of MI-AC and its control samples (AC and LI-AC) were investigated to summarize the porosity development mechanisms of three preparation procedures. Fig. 1 shows the surface morphology and microstructure of the coal-based activated carbons prepared by three preparation procedures, which are obtained by SEM and HRTEM. Fig. 1(a) shows the micro-morphology of AC obtained by solely physical activation, consisting of a large amount of compact-aggregated structures, which is derived from the raw coal structure (Fig. S3). Fig. 1(b) and (c) further present the TEM images of AC, demonstrating an amorphous carbon framework with small pores distributed. Fig. 1(d)–(f) shows the microstructure information of the typical MI-AC-2

sample by the melt infiltration process and reveal big differences from AC. As shown in Fig. 1(d), MI-AC-2 exhibits a much rougher and etched outer surface than the AC (Fig. 1(a)) which brings the development of porosity. The HRTEM image of MI-AC-2 in Fig. 1(e) appears a puffed carbon framework than that of AC (Fig. 1(c)), which is derived from the embedded iron species. This can be demonstrated by the HRTEM image of the pre-washed MI-AC-2 with iron species enclose (Fig. 1(f)), in which the iron species (black dots) disperse in the carbon framework with a relatively small size distribution (almost less than 5 nm). Removing the iron species by acid washing gives a loosened carbon matrix shown in Fig. 1(e). For demonstrating the melt infiltration effect, the microstructures of LI-AC with a traditional liquid impregnation were also characterized and shown in Fig. 1(g)–(i). As can be seen from Fig. 1(g) and (h), the LI-AC shows a similar microstructure to that of AC without obvious surface erosion and structure expansion. Moreover, the HRTEM image of the pre-washed LI-AC sample (Fig. 1(i)) demonstrates much larger iron species domain (up to 30 nm) enclosed onto carbon framework. Thus, we think that the liquid impregnation of FeCl$_3$ into coal structure leads to a surface loading rather than inside dispersion, hence inducing different pore development patterns. The above explanation will be discussed in the following section.
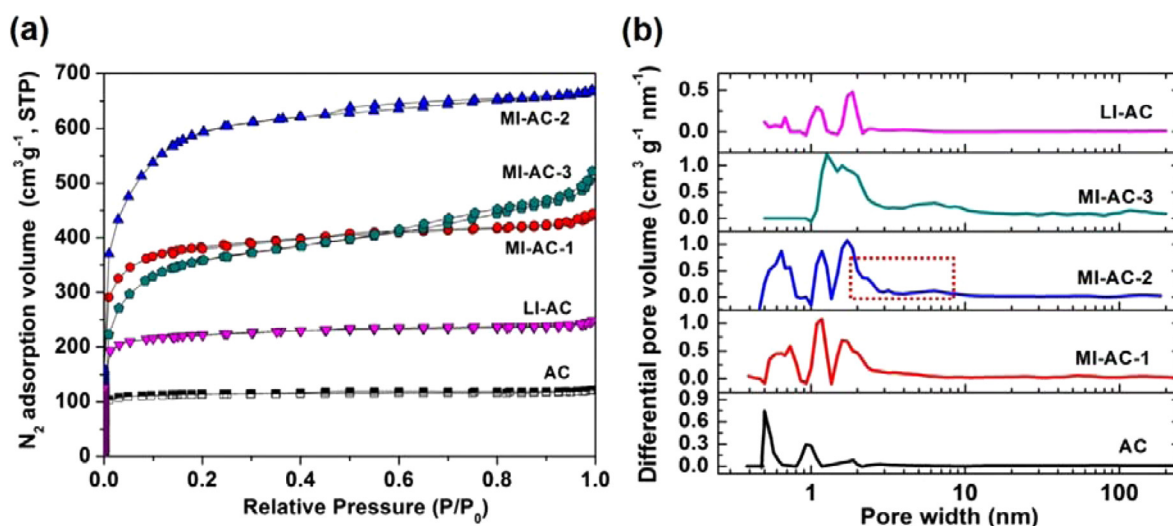
Fig. 2. (a) N_2 adsorption/desorption isotherms of prepared activated carbons. (b) Corresponding DFT pore size distributions of prepared activated carbons.

Table 1
Pore structure parameters of as-prepared activated carbons.

Samples	$FeCl_3$: Coal (mass ratio)	S_{BET} (m^2 g^{-1})	V_{total} (cm^3 g^{-1})	V_{mic} (cm^3 g^{-1})	$V_{mec+mac}$ (cm^3 g^{-1})	D_{ave} (nm)
AC	0	345	0.19	0.16	0.03	2.19
MI-AC-1	1:10	1187	0.69	0.45	0.24	2.31
MI-AC-2	2:10	1872	1.04	0.47	0.57	2.21
MI-AC-3	3:10	1143	0.8	0.28	0.52	2.82
LI-AC	2:10	679	0.38	0.28	0.10	2.26

Fig. 2 shows the nitrogen adsorption/desorption isotherms and the corresponding DFT pore size distributions of various samples. The detailed pore parameters of samples are also summarized in Table 1. As can be observed in Fig. 2(a), all the MI-ACs samples show much higher N_2 adsorption amounts than AC by solely physical activation, which suggests that $FeCl_3$-assisted melt infiltration treatment promoted the porosity development of resulting activated carbons during activation process. More specifically, AC by CO_2-assisted physical activation exhibits a typical Type I adsorption isotherm with steep uptakes below $P/P_0 = 0.1$, confirming the dominant micropore structure [19]. The BET surface area and pore volume of AC are just 345 m^2 g^{-1} and 0.19 cm^3 g^{-1}, respectively. By contrast, the MI-ACs show both higher BET surface areas and pore volumes than those of AC (Table 1). Furthermore, the DFT pore size distributions of MI-ACs show obvious right shifts compared with AC, demonstrating the pore size broadening effect by $FeCl_3$-assisted activation. In addition, the $FeCl_3$ ratio in the coal-$FeCl_3$ mixture also affects the porosity development of MI-ACs. As can be seen in Fig. 2(a) and Table 1, the optimal $FeCl_3$: coal ratio of 2:10 gives the MI-AC-2 sample with the highest specific surface area and pore volume of 1872 m^2 g^{-1} and 1.04 cm^3 g^{-1}, respectively. Overmuch $FeCl_3$ loading may cause serious carbon consumption and consequently trigger pore collapse during activation. Moreover, the optimized MI-AC-2 also shows a hysteresis loop in the amplified N_2 isotherm with P/P_0 from 0.4 to 0.8 (Fig. S4), demonstrating the existence of mesopores, which is consistent with the corresponding pore size distribution (imaginary line box in Fig. 2(b)). Such a hierarchical pore structure of MI-AC-2 has the potential to promote electrolyte ion transfer and storage for the supercapacitor utilization. Moreover, the pore structures of LI-AC (with the same $FeCl_3$ to coal ratio as MI-AC-2) obtained by a liquid impregnation method were also compared in Fig. 2 and Table 1. Despite the increased BET surface area (679 m^2 g^{-1}) and pore volume (0.38 cm^3 g^{-1}) of LI-AC compared with AC, it shows much lower pore parameters than those of MI-ACs, clearly demonstrat-

ing the superiority of melt infiltration method compared with the liquid impregnation method for promoting the porosity development of coal-based activated carbons. It is also worth mentioning that such a melt infiltration strategy just adopts a small amount of melt precursor (only 20 wt% of the coal) to achieve a significant porosity promotion of activated carbons. The BET surface area and pore volume of the as-obtained MI-AC-2 sample are comparable to the commercial and reported coal/biomass-derived activated carbons by chemical activation methods with large amounts of chemical activation agents. A comprehensive comparison between our MI-AC-2 sample and the activated carbons prepared by traditional physical or chemical activation procedures is summarized in Table S3.

To further investigate the crystalline structures of as-obtained activated carbons through various preparation procedures, X-ray diffraction (XRD) and Raman analyses were conducted. As observed in Fig. 3(a), AC exhibits two broad diffraction peaks at *ca.* 24° and 42° assigned as the (002) and (100) reflections of carbon framework [33]. These two peaks in the XRD patterns of MI-ACs and LI-AC become less visible relative to AC, which were ascribed to the presence of abundant pores in MI-ACs and LI-AC, weakening the (002) and (100) peaks [34]. This phenomenon was further confirmed by the Raman spectra in Fig. 3(b). After being calculated, the I_D/I_G of MI-ACs and LI-AC (more than 0.9) is higher than AC (0.73), which demonstrates the increased amorphous/disordered structures existing in the carbon matrix of MI-ACs and LI-AC [35]. Thus, both XRD and Raman results suggest that the activated carbons obtained by $FeCl_3$ treatment (both melt infiltration and liquid impregnation) show more disordered carbon structures than AC by solely physical activation process, which should favorably lead to forming an easily-etched carbon matrix and hence receiving rich porosity during high-temperature activation process, as evidenced by the N_2 adsorption results.

The chemical environment of as-obtained activated carbons was investigated by the X-ray photoelectron spectroscopy (XPS)
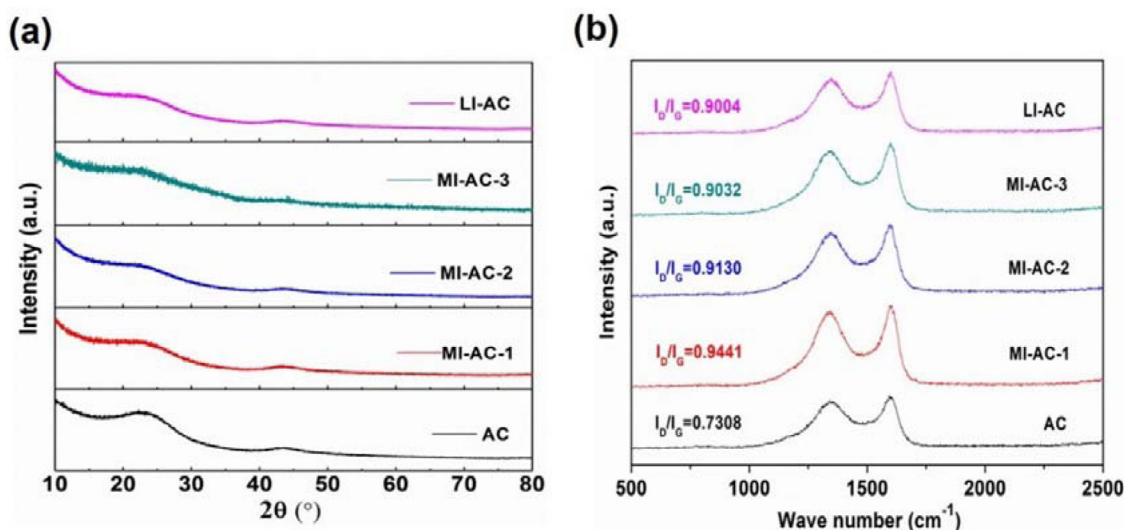
Fig. 3. (a) XRD patterns of prepared activated carbons; (b) Raman spectra of prepared activated carbons.
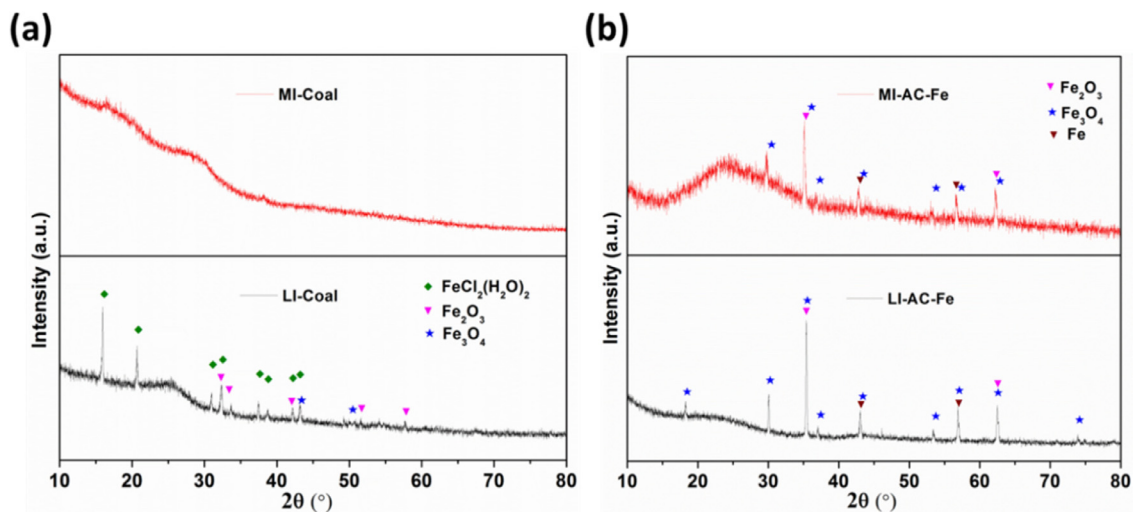

Fig. 4. (a) XRD patterns of MI-Coal and LI-Coal; (b) XRD patterns of MI-AC and LI-AC. (MI-Coal refers to the iron loaded coal precursor obtained by the melt infiltration treatment; LI-Coal refers to the iron loaded coal precursor obtained by the liquid impregnation treatment; MI-AC-Fe and LI-AC-Fe refers to the iron loaded activated carbons after activation treatment and without washing the iron species. The mass ratio of $FeCl_3$ in the $FeCl_3$-coal mixture for both melt infiltration and liquid impregnation is 20% of the coal).

measurements, as shown in Fig. S5 and Table S4. It can be seen from the overall XPS spectra (Fig. S4(a)) that all the tested samples show two peaks of C1s and O1s signals with similar atomic percentages between them (Table S4). Moreover, the high-resolution C1s spectra of all as-obtained activated carbons can be similarly fitted to four component peaks corresponding to C–C (sp^2 carbon) at 285 eV, C–O–R(hydroxyl) at 286.4 eV, –C=O(carbonyl) at 287 eV and O–C=O(carboxyl) at 288.9 eV [36] (Fig. S5(b)). The XPS results demonstrated that the impact of $FeCl_3$ loading on the surface chemistry of resulting activated carbons is negligible.

3.2. Porosity development mechanism by melt infiltration

Hereto, we clearly demonstrated that iron species loading to coal precursors, especially by the melt infiltration process, play a dominant role in the porosity development of resulting activated carbons. To further elucidate the melt infiltration effects, the iron species loaded samples before and after high-temperature activation procedure were investigated by XRD measurements, as shown in Fig. 4. As can be seen from Fig. 4(a) bottom, the LI-Coal sample (the iron loaded coal precursor obtained by the liquid impregnation treatment) exhibits obvious Fe-containing peaks which are assigned to $FeCl_2 \cdot (H_2O)_2$, Fe_2O_3 and Fe_3O_4 phases. These Fe-containing species are ascribed to the low-temperature conversion of $FeCl_3 \cdot (H_2O)_6$ with coal structure during mixing and airy drying. After CO_2-assisted high-temperature activation treatment, the iron species in LI-Coal were transformed to both oxidized Fe species (Fe_2O_3 and Fe_3O_4) and reduced Fe elements under the action of carbon, which can be demonstrated by the XRD pattern of LI-AC-Fe sample (Fig. 4(b) bottom). Compared with LI-Coal, MI-Coal obtained by the melt infiltration treatment shows a great difference in the XRD pattern (Fig. 4(a) top), which just presents broad amorphous carbon features with no Fe-related crystalline peaks. However, the above result does not mean there are no Fe-species in the MI-Coal sample, which can be proved by the XRD pattern of MI-AC-Fe in Fig. 4(b) top. Similar Fe-containing species can be detected in MI-AC-Fe relative to LI-AC-Fe, suggesting the successful loading of $FeCl_3$ into the coal structure by melt infiltration treatments. The differences of XRD patterns between MI-Coal and LI-Coal (Fig. 4(a) top and bottom) are due to the different $FeCl_3$
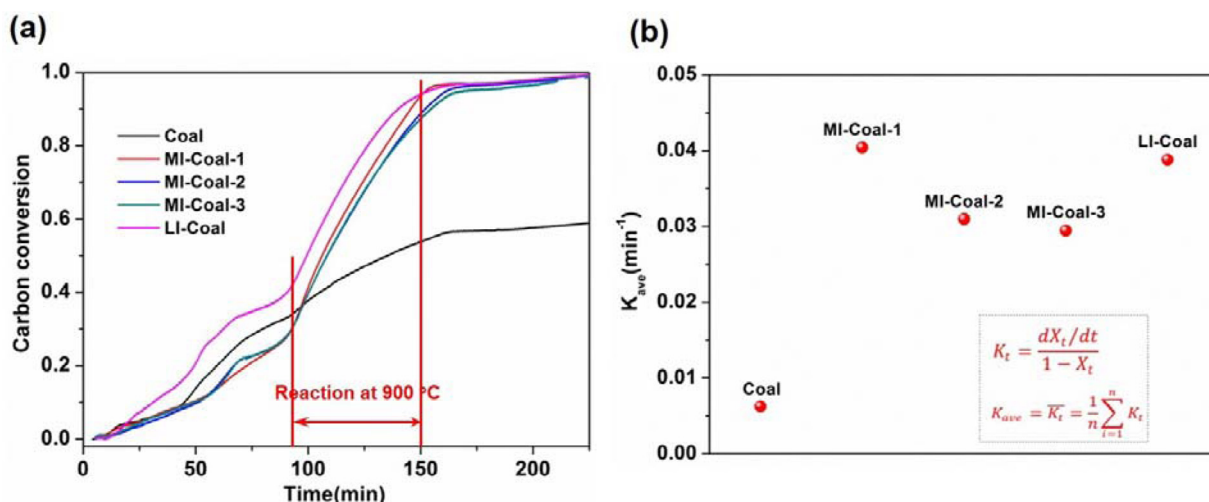
Fig. 5. (a) TGA profiles of various coal samples under simulated CO_2-assisted activation process (10 °C min^{-1} up to 900 °C; holding 1 h in CO_2 and N_2 atmosphere with a flow rate of 100 mL min^{-1}; volume ratio of $CO_2:N_2 = 2:3$); (b) average reaction rates in from 90 to 150 min.
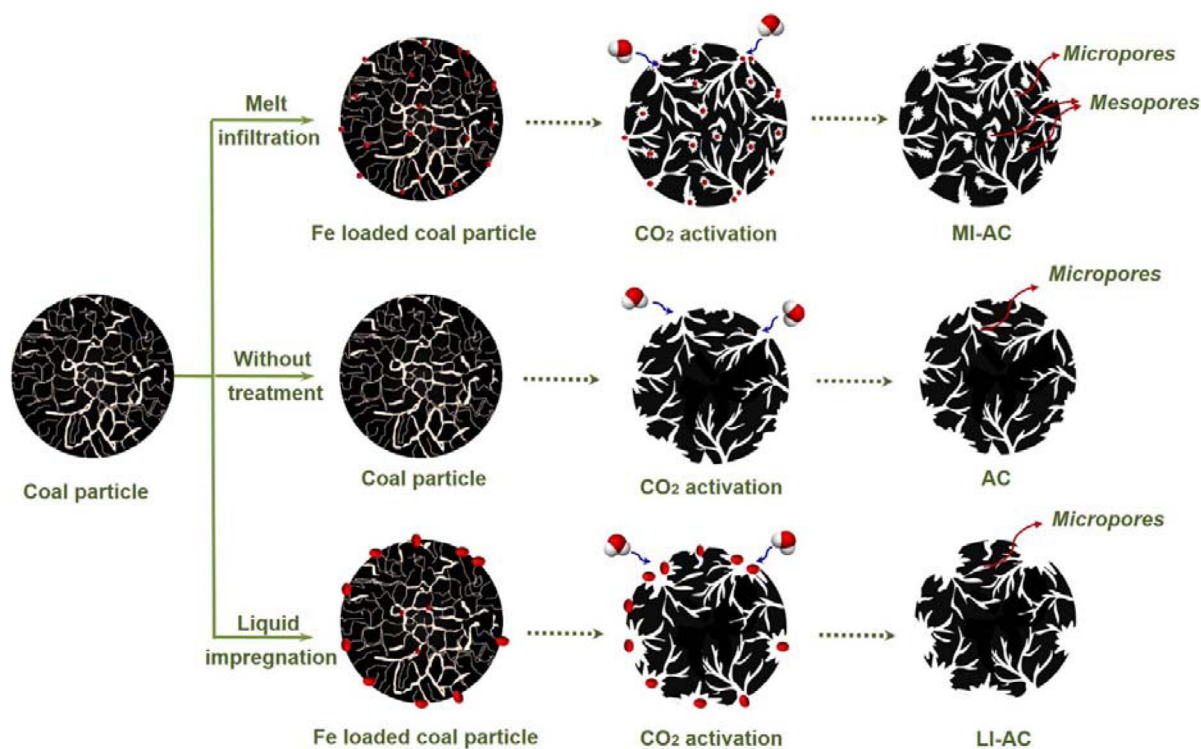

Fig. 6. A schematic illustration of the porosity development mechanism by various strategies.

loading mechanism between melt infiltration and liquid impregnation. For the melt infiltration process, anhydrous $FeCl_3$ and coal power were homogeneously ground in a mortar, vacuumized and then sealed in a glass vial. The mixture was then heated up to the temperature slightly higher than the melting temperature of $FeCl_3$ ($T_m = \sim 310$ °C) [37], which allowed the capillary infiltration of $FeCl_3$ by coal inner pores. This method ensures the formation of small Fe-containing crystals uniformly dispersed and confined in the coal inner structure. By contrast, the traditional liquid impregnation of $FeCl_3$ with coal commonly leads to aggregated Fe species loading onto the outer surface of coal framework. Thus, it could be understood that no obvious Fe-related species be detected in the XRD pattern of MI-Coal due to the encapsulation of Fe species by coal structure while visible Fe-related peaks can be observed in the XRD pattern of LI-Coal due to the outer surface loading.

The more dispersible and smaller iron species induced by melt infiltration than that of liquid impregnation can also be demonstrated by the above-mentioned TEM results of MI-AC-Fe and LI-AC-Fe (Fig. 1(f) and (i)). Moreover, the amount of the entrapped iron species was verified by TGA analysis during air atmosphere, as shown in Fig. S6. As depicted in Fig. S6, despite the similar amount of iron species entrapped into various ACs, LI-AC-Fe possesses the higher amount of iron species (32.9%) compared with those in MI-AC-Fe (29.4%), which is consistent with the XRD analyses in Fig. 4(b).

The dispersible and small iron species confined in the coal structure induced by the melt infiltration method favorably promotes the pore formation reactions during subsequent activation process between CO_2 and coal structure. To further explore the mechanism underlying the influence of $FeCl_3$ in coal
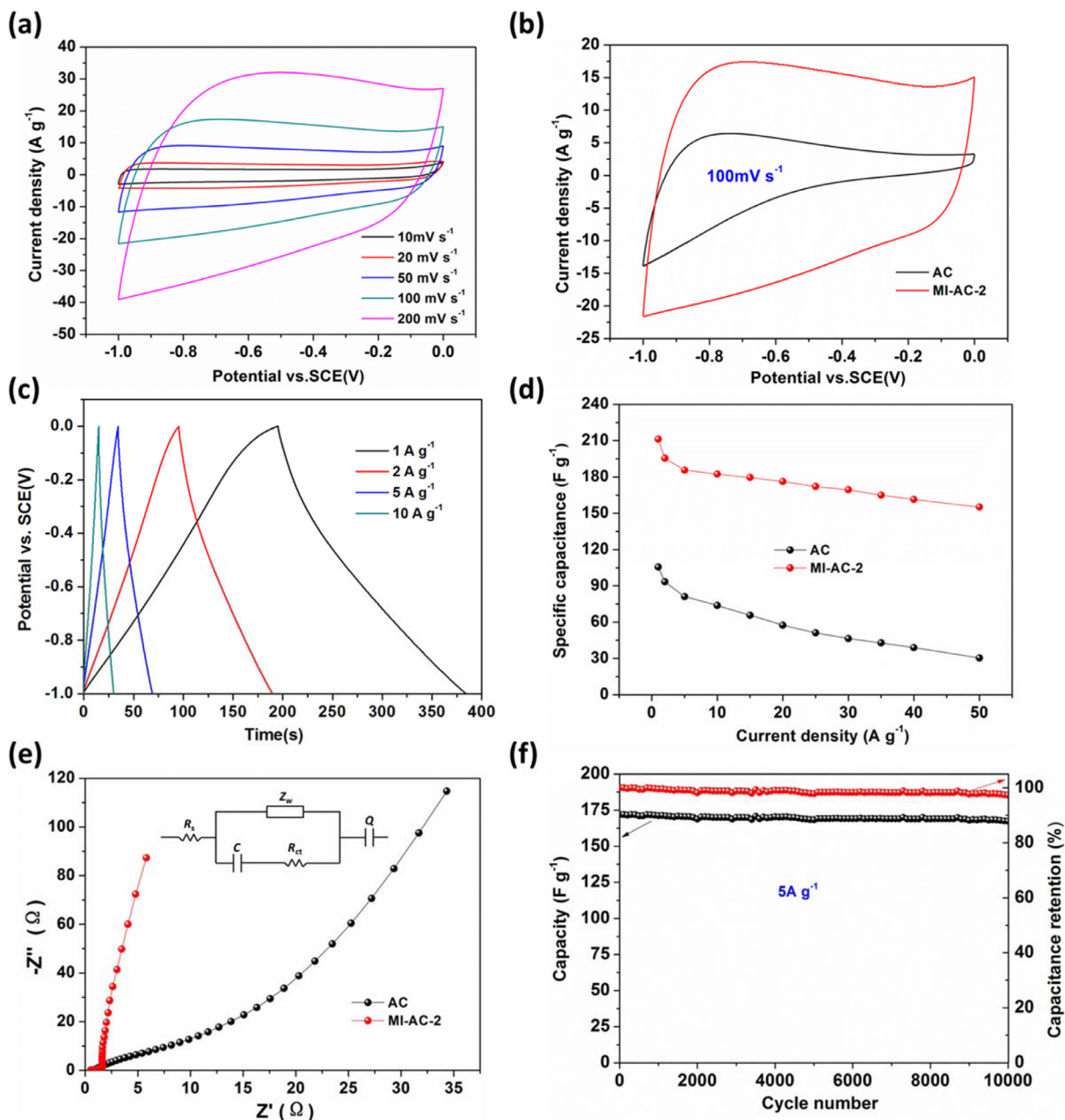
Fig. 7. Electrochemical performances of typical samples in 6 M KOH electrolyte. (a) CV curves of MI-AC-2 at the scan rates of 10 to 200 mV s^{-1}; (b) CV curves of MI-AC-2 and AC at the scan rates of 100 mV s^{-1}; (c) galvanostatic charge–discharge curves of MI-AC-2 at different current densities; (d) gravimetric capacitances of MI-AC-2 and AC at different current densities; (e) Nyquist plots of MI-AC-2 and AC, inset shows the fitting equivalent circuit model; (f) cycling stability of the MI-AC-2 at a current density of 5 A g^{-1}.

precursor on the pore structure of resulting activated carbons, thermogravimetric analyses (TGA) of various coal precursors was conducted under the simulated CO_2-assisted activation procedure. The carbon conversion and average conversion rates (K_{ave}) during temperature-rise process are shown in Fig. 5. It can be seen that the carbon conversion and K_{ave} of iron-loaded coal samples are much higher than pure coal, which suggests that a small amount of iron species loading significantly promote the etching reaction between CO_2 and coal structure to generate rich pores. The promotion effects have been studied and demonstrated by previous literature regarding the coal gasification reactions in which transition metal oxides (such as Fe_2O_3 [38], K_2CO_3 [39] and NiO [40], *etc.*) enhance the gasification reactivity of coal/biomass with CO_2 or H_2O.

Based on all the above-mentioned structural characterization results, we herein summarize the porosity development of the Zhundong coal-based activated carbon by melt infiltration of anhydrous $FeCl_3$ into coal structure assisted with a CO_2 physical activation as an illustration in Fig. 6: (1) melt infiltration of anhydrous $FeCl_3$ into the coal framework endows the $FeCl_3$-coal mixture with dispersed and confined Fe nanocrystals in the coal inner structure; (2) during the CO_2 physical activation process, the confined and dispersible Fe species play the dual role of activating catalysts for the promotion of CO_2 etching reaction with coal skeleton and pore-forming templates for some mesopores (as evidenced by the hysteresis loop in the N_2 adsorption isotherm). Thereby, the optimized MI-AC-2 sample with 20% $FeCl_3$ additive shows a partially hierarchical pore structure with a high surface

area and a large pore volume. By contrast, the solely physical activation endures a much lower reaction reactivity between coal structure and CO_2 molecules, thus leading to the resulting AC with low porosity. Moreover, although the traditional liquid impregnation of $FeCl_3$ with coal also promotes the reaction between coal structure and CO_2 molecules and increases the porosity compared with solely physical activation, the aggregated Fe species loading onto the outer surface of coal framework cause an outside-in etching by CO_2 molecules with lowly-dispersible Fe-containing active sites, resulting in the LI-AC with much inferior pore structure relative to MI-AC.

To further verify the porosity development effects of such melt infiltration method on other kind of low-rank coals, we employed another kind of low-rank coal, namely Huolinhe lignite (HLH) from Chinese Inner Mongolia Huolinhe region, to prepare activated carbons. The industrial, ultimate analysis and ash analysis are shown in Tables S5 and S6, demonstrate its lignite properties. Through the same preparation procedures as MI-AC-2 (mineral removal, melt infiltration of 20 wt% $FeCl_3$ into coal and subsequent CO_2-assisted physical activation), the resulting activated carbon (denoted as HLH-MI-AC) also shows a much increased porosity comparing with the activated carbon (HLH-AC) by solely physical activation (detailed pore characterization seeing Fig. S7 and Table S7), directly demonstrating the wide adaptability of such melt infiltration method for promoting porosity development of coal-based activated carbons.

3.3. Supercapacitive performances of typical samples

Evaluated as supercapacitor electrode materials, the as-obtained MI-AC-2 with well-developed pore structure was deemed to have high capacitance, good rate capability and cycling stability. Fig. 7 shows the electrochemical performances of MI-AC-2 as well as the control sample AC in a three-electrode system using 6 M KOH as the electrolyte. It can be found from Fig. 7(a) that the cyclic voltammetry (CV) curves of the MI-AC-2 electrode retain nearly rectangular shapes with the increase of scan rates from 10 mV s^{-1} to 200 mV s^{-1}, indicating well ion transport in the electrode at high charge–discharge rates [7]. However, the AC electrode presents distorted CV curves (Fig. S8(a)), implying the deteriorative electrolyte ion transfer and adsorption [41,42]. Fig. 7(b) presents the CV curves of MI-AC-2 and AC electrodes at 100 mV s^{-1}, in which the much better and bigger rectangular area of MI-AC-2 electrode indicating the much superior capacitive performance of MI-AC-2 than that of AC. Figs. 7(c) and S8(b) show the galvanostatic charge–discharge (GC) curves of the MI-AC-2 and AC electrodes at different current densities. Compared with the AC electrode, the MI-AC-2 electrode shows almost isosceles triangular shape and demonstrates good charge and discharge characteristics for electric double layer capacitors (EDLCs). Fig. 7(d) shows the specific capacitances of AC and MI-AC-2 electrodes at different current densities from which MI-AC-2 electrode has much higher capacitances relative to AC. The gravimetric capacitance of MI-AC-2 is ~211 F g^{-1} at 1 A g^{-1}. Furthermore, at a high current rate of 20 A g^{-1}, the MI-AC-2 electrode still exhibits a specific capacitance of 176 F g^{-1} with slight capacitance decay. Even at a current density of 50 A g^{-1}, the specific capacitance is still as much as 155 F g^{-1}, indicating a rapid charge–discharge capability. The electrochemical performance of the LI-AC is also compared in Fig. S8(c) and (d), which exhibits a capacitive performance between MI-AC-2 and AC. Thus, it can be concluded that the capacitive performances of the as-obtained Zhundong coal-based activated carbons show good positive correlations with their pore parameters. Moreover, the electrode densities were calculated by selecting a homogeneous carbon film with 1 cm^2 and measuring its mass and thickness (seeing Fig. S9). Then, the volumetric capacitances

of prepared electrodes were calculated, as depicted in Fig. S10. MI-AC-2 electrode still exhibits relatively high volumetric capacitances compared to AC and LI-AC, though density of MI-AC-2 electrode (0.54 g cm^{-3}) is relatively lower than AC (0.67 g cm^{-3}) and LI-AC (0.57 g cm^{-3}). Electrochemical impedance spectroscopy (EIS) is an effective method for studying the fundamental behavior of carbon materials in EDLCs [43–45]. Fig. 7(e) shows the Nyquist plots of the AC and MI-AC-2 electrodes of the frequency range from 10 mHz to 100 KHz. As can be seen, the MI-AC-2 electrode displays a relatively small semicircle radius for the impedance loops in the high-frequency region, indicating small charge transfer resistance. The fitting equivalent circuit model obtained by using the coupled nonlinear Schrodinger equation (CNLS) method is shown in Fig. 7(e), and the fitting results are listed in Table S8. The MI-AC-2 electrode exhibits a low resistance of 0.3513 Ω. Moreover, MI-AC-2 electrode presents a much higher slope in the low-frequency region than that of AC electrode, indicating the preferable ion transport dynamic of MI-AC-2 electrode relative to AC electrode, which is consistent with the above CV and GC results. Fig. 7(f) further shows the cycling stability of MI-AC-2 electrode at a current density of 5 A g^{-1}. The MI-AC-2 electrode delivers a specific capacitance of 179 F g^{-1} at a current density of 5 A g^{-1} and maintains about 97% of the capacitance after 10,000 cycles, demonstrating its excellent cycling stability.

4. Conclusion

In summary, we have demonstrated a novel melt infiltration method to greatly promote the porosity development of activated carbons by employing Chinese large-reserve Zhundong coal as precursor. The preparation is achieved by the melt infiltration of anhydrous $FeCl_3$ into the coal framework and subsequent CO_2-assisted physical activation during which the dispersed and confined iron species play the dual role of pore-forming templates and activating catalysts. The MI-AC-2 obtained possesses a partially hierarchical pore structure with surface area five times more than that of the activated carbon produced by solely physical activation. Such well-developed pore structure endows the MI-AC-2 with excellent supercapacitive performances in terms of high capacitances, good rate capability and excellent cycling stability. This work provides a simple and scalable melt infiltration method for developing high-performance coal-based activated carbons with adding a small amount of metal precursor and holds potentials for industrial scale-up and applications.

Supplementary materials

Supplementary material associated with this article can be found, in the online version, at doi:10.1016/j.jtice.2018.06.014.

References

[1] Sun F, Gao JH, Yang YQ. One-step ammonia activation of Zhundong coal generating nitrogen-doped microporous carbon for gas adsorption and energy storage. Carbon 2016;109:747–54.
[2] Zhu YW, Gao JH, Li Y. Preparation of activated carbons for SO$_2$, adsorption by CO$_2$, and steam activation. J Taiwan Inst Chem Eng 2012;43:112–19.
[3] Sun F, Liu X, Gao JH. Highlighting the role of nitrogen doping in enhancing CO$_2$ uptake onto carbon surfaces: a combined experimental and computational analysis. J Mater Chem A 2016;4:18248–52.
[4] Alabadi A, Razzaque S, Yang Y. Highly porous activated carbon materials from carbonized biomass with high CO$_2$ capturing capacity. Chem Eng J 2015;281:606–12.

[5] Li W, Ding Y, Zhang W, Shu Y, Zhang L, Yang F. Lignocellulosic biomass for ethanol production and preparation of activated carbon applied for super-capacitor. J Taiwan Inst Chem Eng 2016;64:166–72.

[6] Li BL, Li ZS, Zhang L. Facile synthesis of polyaniline nanofibers/porous carbon microspheres composite for high performance supercapacitors. J Taiwan Inst Chem Eng 2017;81:465–71.

[7] Wang L, Mu G, Tian CG. Porous graphitic carbon nanosheets derived from cornstalk biomass for advanced supercapacitors. ChemSusChem 2013;6:880–9.

[8] Zhang Y, Park SJ. Incorporation of RuO_2 into charcoal-derived carbon with controllable microporosity by CO_2 activation for high-performance supercapacitor. Carbon 2017;122:287–97.

[9] Liu XJ, Yang XQ, Liu C, Peng C. Low-temperature catalytic steam reforming of toluene over activated carbon supported nickel catalysts. J Taiwan Inst Chem Eng 2016;65:233–41.

[10] Guo JX, Liang J, Chu YH. Influence of Ni species of Ni/AC catalyst on its desulfurization performance at low temperature. Chinese J Catal 2010;31:278–82.

[11] Sun YB, Cao CY, Liu C. Nitrogen-doped hollow carbon spheres derived from amination reaction of fullerene with alkyl diamines as a carbon catalyst for hydrogenation of aromatic nitro compounds. Carbon 2017;125:139–45.

[12] Hardwick LJ, Hahn M, Ruch P. An in situ Raman study of the intercalation of supercapacitor-type electrolyte into microcrystalline graphite. Electrochim Acta 2006;52:675–80.

[13] Xing W, Qiao SZ, Ding RG. Superior electric double layer capacitors using ordered mesoporous carbons. Carbon 2006;44:216–24.

[14] And MK, Jaroniec M, And RR. Characterization of ordered mesoporous carbons synthesized using MCM-48 silicas as templates. J Phys Chem B 2000;104:7960–8.

[15] Miao F, Shao C, Li X. Polyaniline-coated electrospun carbon nanofibers with high mass loading and enhanced capacitive performance as freestanding electrodes for flexible solid-state supercapacitors. Energy 2016;95:233–41.

[16] Thompson BC, Fréchet JM. Polymer-fullerene composite solar cells. Angew Chem 2010;47:58–77.

[17] Stoller MD, Park S, Zhu Y. Graphene-based ultracapacitors. Nano Lett 2008;8:3498–502.

[18] Li X, Cai W, An J. Large-area synthesis of high-quality and uniform graphene films on copper foils. Science 2009;324:1312–14.

[19] Sun F, Gao JH, Liu X. Controllable nitrogen introduction into porous carbon with porosity retaining for investigating nitrogen doping effect on SO_2 adsorption. Chem Eng J 2016;290:116–24.

[20] Zhai Y, Dou Y, Zhao D. Carbon materials for chemical capacitive energy storage. Adv Mater 2011;23:4828–50.

[21] Sun F, Gao JH, Pi X X. High performance aqueous supercapacitor based on highly nitrogen-doped carbon nanospheres with unimodal mesoporosity. J Power Sources 2017;337:189–96.

[22] Wang K, Cao Y, Wang X. Nickel catalytic graphitized porous carbon as electrode material for high performance supercapacitors. Energy 2016;101:9–15.

[23] He XJ, Zhang HB, Zhang H. Direct synthesis of 3D hollow porous graphene balls from coal tar pitch for high performance supercapacitors. J Mater Chem A 2014;46:19633–40.

[24] Li YT, Pi Y T, Lu LM. Hierarchical porous active carbon from fallen leaves by synergy of K_2CO_3, and their supercapacitor performance. J Power Sources 2015;299:519–28.

[25] Foo KY, Hameed BH. Preparation and characterization of activated carbon from sunflower seed oil residue via microwave assisted K_2CO_3 activation. Bioresour Technol 2010;102:9794–9.

[26] Ma GF, Yang Q, Sun KJ. Nitrogen-doped porous carbon derived from biomass waste for high-performance supercapacitor. Bioresour Technol 2015;197:137–42.

[27] Elmouwahidi A, Bailón-García E, Pérez-Cadenas AF. Activated carbons from KOH and H_3PO_4-activation of olive residues and its application as supercapacitor electrodes. Electrochim Acta 2017;229:219–28.

[28] Zhang K, Li Y, Wang ZH. Pyrolysis behavior of a typical Chinese sub-bituminous Zhundong coal from moderate to high temperatures. Fuel 2016;185:701–8.

[29] Gao MQ, Yang ZY, Wang YL. Impact of calcium on the synergistic effect for the reactivity of coal char gasification in H_2O/CO_2 mixtures. Fuel 2017;189:312–21.

[30] Li D, Ding LX, Chen H. Novel nitrogen-rich porous carbon spheres as a high-performance anode material for lithium-ion batteries. J Mater Chem A 2014;39:16617–22.

[31] Wang YL, Zhu SH, Gao MQ. A study of char gasification in H_2O and CO_2 mixtures: role of inherent minerals in the coal. Fuel Process Technol 2016;141:9–15.

[32] Molina A, Mondragón F. Reactivity of coal gasification with steam and CO_2. Fuel 1998;77:1831–9.

[33] Liang X, Liu HY, Yan J. Structural order and dielectric properties of coal chars. Fuel 2014;137:164–71.

[34] Li ZJ, Zhang WY, Li YC. Activated pyrene decorated graphene with enhanced performance for electrochemical energy storage. Chem Eng J 2017;334:845–54.

[35] Li Q, Yang JP, Feng D. Facile synthesis of porous carbon nitride spheres with hierarchical three-dimensional mesostructures for CO_2 capture. Nano Res 2010;3:632–42.

[36] Lee WH, Lee JG, Reucroft PJ. XPS study of carbon fiber surfaces treated by thermal oxidation in a gas mixture of $O_2/(O_2+N_2)$. App Surf Sci 2001;171:136–42.

[37] Fan YR, Zhao ZB, Zhou Q. Nitrogen-doped carbon microfibers with porous textures. Carbon 2013;58:128–33.

[38] Huang YQ, Yin XL, Wu CZ. Effects of metal catalysts on CO_2 gasification reactivity of biomass char. Biotechnol Adv 2009;27:568–72.

[39] Kopyscinski J, Rahman M, Gupta R. K_2CO_3 catalyzed CO_2 gasification of ash-free coal. Interactions of the catalyst with carbon in N_2 and CO_2 atmosphere. Fuel 2014;117:1181–9.

[40] Hurley S, Li H, Xu CC. Effects of impregnated metal ions on air/CO_2-gasification of woody biomass. Bioresour Technol 2010;101:9301–7.

[41] Raymundo-Piñero E, Cadek M, Béguin F. Tuning carbon materials for supercapacitors by direct pyrolysis of seaweeds. Adv Funct Mater 2009;19:1032–9.

[42] Liu HJ, Wang J, Wang CX. Ordered hierarchical mesoporous/microporous carbon derived from mesoporous titanium-carbide/carbon composites and its electrochemical performance in supercapacitor. Adv Energy Mater 2011;1:1101–8.

[43] He XJ, Geng YJ, Qiu JS. Effect of activation time on the properties of activated carbons prepared by microwave-assisted activation for electric double layer capacitors. Carbon 2010;48:1662–9.

[44] Li W, Zhang F, Dou YQ. A self-template strategy for the synthesis of mesoporous carbon nanofibers as advanced supercapacitor electrodes. Adv Energy Mater 2011;1:382–6.

[45] He CN, Wu S, Zhao NQ. Carbon-encapsulated Fe_3O_4 nanoparticles as a high-rate lithium ion battery anode material. ACS Nano 2013;7:4459–69.